A&A 612, A117 (2018)
https://doi.org/10.1051/0004-6361/201732067

Astronomy & Astrophysics

Exploring the ^{13}CO/C^{18}O abundance ratio towards Galactic young stellar objects and HII regions

M. B. Areal[1], S. Paron[1,2], M. Celis Peña[1], and M. E. Ortega[1]

[1] CONICET-Universidad de Buenos Aires, Instituto de Astronomía y Física del Espacio CC 67, Suc. 28, 1428 Buenos Aires, Argentina
e-mail: sparon@iafe.uba.ar
[2] Universidad de Buenos Aires, Facultad de Arquitectura, Diseño y Urbanismo, Buenos Aires, Argentina

Received 9 October 2017 / Accepted 22 December 2017

ABSTRACT

Aims. Determining molecular abundance ratios is important not only for the study of Galactic chemistry, but also because they are useful to estimate physical parameters in a large variety of interstellar medium environments. One of the most important molecules for tracing the molecular gas in the interstellar medium is CO, and the ^{13}CO/C^{18}O abundance ratio is usually used to estimate molecular masses and densities of regions with moderate to high densities. Nowadays isotope ratios are in general indirectly derived from elemental abundances ratios. We present the first ^{13}CO/C^{18}O abundance ratio study performed from CO isotope observations towards a large sample of Galactic sources of different natures at different locations.

Methods. To study the ^{13}CO/C^{18}O abundance ratio, we used ^{12}CO $J = 3-2$ data obtained from the CO High-Resolution Survey, ^{13}CO and C^{18}O $J = 3-2$ data from the ^{13}CO/C^{18}O ($J = 3-2$) Heterodyne Inner Milky Way Plane Survey, and some complementary data extracted from the *James Clerk Maxwell* Telescope database. We analyzed a sample of 198 sources composed of young stellar objects (YSOs), and HII and diffuse HII regions as catalogued in the Red MSX Source Survey in $27\overset{\circ}{.}5 \leq l \leq 46\overset{\circ}{.}5$ and $|b| \leq 0\overset{\circ}{.}5$.

Results. Most of the analyzed sources are located in the galactocentric distance range 4.0–6.5 kpc. We found that YSOs have, on average, lower ^{13}CO/C^{18}O abundance ratios than HII and diffuse HII regions. Taking into account that the gas associated with YSOs should be less affected by the radiation than in the case of the others sources, selective far-UV photodissociation of C^{18}O is confirmed. The ^{13}CO/C^{18}O abundance ratios obtained in this work are systematically lower than those predicted from the known elemental abundance relations. These results will be useful in future studies of molecular gas related to YSOs and HII regions based on the observation of these isotopes.

Key words. ISM: abundances – ISM: molecules – Galaxy: abundances – HII regions – stars: formation

1. Introduction

Studying molecular abundances towards different Galactic sources and their association with the surrounding interstellar medium is a very important issue in astrophysics. To study the chemical evolution of the Galaxy, and hence the physical processes related to the chemistry, it is crucial to have accurate values of the molecular abundances.

It is well known that carbon monoxide is the second most abundant molecule in the Universe, and the rotational transitions of ^{12}C^{16}O (commonly ^{12}CO) are easily observable. Our knowledge of the molecular gas distribution along the Galaxy comes mainly from the observation of this molecular species and its isotopes, such as ^{13}C^{16}O (^{13}CO) and ^{12}C^{18}O (C^{18}O). Any study involving molecular gas traced by the CO isotopes needs molecular abundance relations to derive physical and chemical parameters.

Wilson & Rood (1994) and Wilson (1999) presented one of the most complete and most often used works on interstellar abundances focused on chemical elements. With regard to C and O, and hence to CO and its isotopes, most of the works in the literature that have to assume an abundance ratio concerning CO use the values from Wilson's papers. Wilson & Rood (1994) have shown that ^{12}C/^{13}C and ^{16}O/^{18}O depend on the distance to the Galactic center. These relations were obtained mainly from observations of H_2CO absorption lines because, as the authors mention, direct measurements of CO presented some problems, such as a lack of surveys with a complete set of CO isotopes with good S/N. Later, Milam et al. (2005) studied ^{12}C/^{13}C through the $N = 1-0$ transition of the CN radical and also found the same dependency on the galactocentric distance. In addition to this dependency on distance to the Galactic center, the isotope abundance ratios can present variations along the same molecular cloud. This is the case for the ^{12}CO/^{13}CO abundance ratio, which may vary considerably within the same molecular cloud due to chemical fractionation and isotope-selective chemical processes (see Szűcs et al. 2014 and references therein).

Concerning the ^{13}CO/C^{18}O abundance ratio, early works of Dickman et al. (1979) and Langer et al. (1980) have shown spatial gradients from the edge to the center of molecular clouds. More recently, direct observations of the ^{12}CO, ^{13}CO, and C^{18}O lines have been used to determine abundance ratios and their relation with far-UV radiation towards different regions in molecular clouds (Lin et al. 2016; Kong et al. 2015; Shimajiri et al. 2014), showing that the ^{13}CO/C^{18}O abundance ratio may exhibit significant spatial variations. These studies show that the abundance ratios can depend not only on galactocentric distances, but also on the type of the observed source and its surroundings. Young stellar objects (YSOs) and HII regions can be useful targets to study this issue because the molecular gas at their surroundings are affected by far-UV radiation, jets, winds, and outflows. Studies are needed towards a large sample of these objects using the CO $J = 3-2$ line, which has a critical density $\gtrsim 10^4$ cm^{-3} and nowadays is extensively used to observe their surroundings.

It is important to mention that if one needs to assume an abundance ratio between molecular isotopes, the best solution would be to use a value that has been derived directly from the molecular species and not from the ratio between the elements that compose the molecules. In the case of the ^{13}CO/C^{18}O abundance ratio, most of the works in the literature perform a double ratio from the Wilson ^{12}C/^{13}C and ^{16}O/^{18}O expressions, due to (as mentioned above) a lack of CO isotope surveys with good S/N that cover large areas in the Galaxy.

At present there are some surveys of ^{12}CO, ^{13}CO, and C^{18}O $J = 3-2$ with good S/N that allow us to perform abundance estimates towards many sources of different nature in the Galaxy. We present here a study of the ^{13}CO/C^{18}O abundance ratio towards a large sample of YSOs and HII regions in a region of about 20° × 1° at the first Galactic quadrant. This is the first large survey of ^{13}CO/C^{18}O abundance ratios, and it was performed in order to test the known CO abundance relations using a modern data set and to explore how the abundance ratios depend not only on the distance to the Galactic center, but also on the type of source or region observed.

2. Data and sources selection

The data of the CO isotopes were extracted from two public databases performed with the 15 m *James Clerk Maxwell* Telescope (JCMT) in Hawaii. The ^{12}CO $J = 3-2$ data were obtained from the CO High-Resolution Survey (COHRS) with an angular and spectral resolution of 14″ and 1 km s^{-1} (see Dempsey et al. 2013). The data of the other CO isotopes were obtained from the ^{13}CO/C^{18}O ($J = 3-2$) Heterodyne Inner Milky Way Plane Survey (CHIMPS), which have an angular and spectral resolution of 15″ and 0.5 km s^{-1} (Rigby et al. 2016). The intensities of both sets of data are on the T_A^* scale, and we used the mean detector efficiency $\eta_{\rm mb} = 0.61$ for the ^{12}CO, and $\eta_{\rm mb} = 0.72$ for the ^{13}CO and C^{18}O to convert T_A^* to main beam brightness temperature ($T_{\rm mb} = T_A^*/\eta_{\rm mb}$) (Buckle et al. 2009).

Taking into account that the CHIMPS survey covers the Galactic region in $27\overset{\circ}{.}5 \leq l \leq 46\overset{\circ}{.}5$ and $|b| \leq 0\overset{\circ}{.}5$, we selected all sources catalogued as YSOs, and selected HII and diffuse HII regions lying in this area from the Red MSX Source Survey (Lumsden et al. 2013), which is the largest statistically selected catalogue of young massive protostars and HII regions to date. Figure 1 shows the 198 sources among YSOs (blue crosses), HII regions (red circles), and diffuse HII regions (green circles). This source classification, and the separation from other kinds of sources, was done by Lumsden et al. (2013) using several multiwavelength criteria. To classify the sources the authors combined near- and mid-infrared color criteria, analysis of spectral energy distributions, near-infrared spectroscopy, analysis of radio continuum fluxes and maser emission, and comparisons with other published lists of sources and catalogues. In addition, the morphology of the emission at different wavelengths was also analyzed. For example, sources with stronger emission at 12 μm than at either 8 μm or 14 μm are often extended and classified as diffuse HII regions. Lumsden et al. (2013) note that the final source classification was decided individually for every source. What it is important for our work is that the classification presented in the Red MSX Source Survey differentiates efficiently between two classes of stellar objects: the youngest (YSOs) and the more evolved (HII regions). The "HII region" category can include ultracompact, compact, and point-like HII regions, while the "diffuse HII region" category refers to extended and likely more evolved HII regions.

At the Galactic longitude range covered by CHIMPS, the COHRS survey is restricted to Galactic latitudes of $|b| \leq 0\overset{\circ}{.}25$. Thus, the ^{12}CO data for sources lying in $|b| \geq 0\overset{\circ}{.}25$ and $|b| \leq 0\overset{\circ}{.}5$ were obtained from the JCMT database[1]. In these cases we used the reduced data.

The spectra of each isotope were extracted from the position of each catalogued source in the Red MSX Source Survey. Given that we need the emission from the three isotopes to obtain the ^{13}CO and C^{18}O column densities ($N(^{13}$CO) and N(C^{18}O)) and then the abundance ratio ($X^{13/18} = N(^{13}$CO)/N(C^{18}O)), in the cases where some isotopes do not present emission above the noise level in the surveys, we checked in the JCMT database whether there are observing programs around the source coordinate other than those used to perform the surveys. In the affirmative case, we investigated these data in order to find the missing spectra.

The data were visualized and analyzed with the Graphical Astronomy and Image Analysis Tool (GAIA)[2] and with tools from the Starlink software package (Currie et al. 2014) such as the Spectral Analysis Tool (Starlink SPLAT-VO). The typical rms noise levels of the spectra, in units of T_A^*, are 0.25, 0.35, and 0.40 K for ^{12}CO, ^{13}CO, and C^{18}O, respectively.

3. Results

From the sample of 198 sources lying in the analyzed region (see Fig. 1), we obtained spectra from the three CO isotopes in 114 cases. Table A.1 presents the line parameters obtained from Gaussian fits to the spectra of each CO isotope, also including the velocity-integrated line emission in the case of ^{13}CO and C^{18}O. The assigned number, and the source designation and its classification from the Red MSX Source Survey are included in Cols. 1, 2, and 3. For simplicity, errors are not included in the table. In the case of ^{12}CO and ^{13}CO the typical errors (the formal 1σ value for the model of the Gaussian line shape) in T_{mb} are between 5% and 10%, while the typical error in this parameter for C^{18}O ranges from 10% to 20%. The integrated line emission has typical errors of 5–10% and 10–20% for ^{13}CO and C^{18}O, respectively. All the C^{18}O spectra, and most of the ^{13}CO spectra, present only one component along the velocity axis, which represents the emission related to the catalogued source, defining in this way its central velocity ($v_{\rm LSR}$). In several cases this velocity could be checked with methanol and/or ammonia maser emission catalogued in the Red MSX Source Survey. When the ^{12}CO spectrum of any source presented several velocity components, we selected the one coinciding with the $v_{\rm LSR}$ measured from the other isotopes.

Given that the galactocentric distance of the sources is an important parameter to take into account in order to study the abundances (Wilson & Rood 1994), it is also included in Table A.1 (Col. 4). Most of the sources have catalogued distances in the Red MSX Source Survey that were used to estimate the corresponding galactocentric distance. When a distance was not available in the Red MSX Source Survey, we derived it from the C^{18}O central velocity ($v_{\rm LSR}^{18}$) using the Galactic rotation model of

[1] http://www.cadc-ccda.hia-iha.nrc-cnrc.gc.ca/en/jcmt/

[2] GAIA is a derivative of the SkyCat catalogue and image display tool, developed as part of the VLT project at ESO. SkyCat and GAIA are free software products under the terms of the GNU copyright.

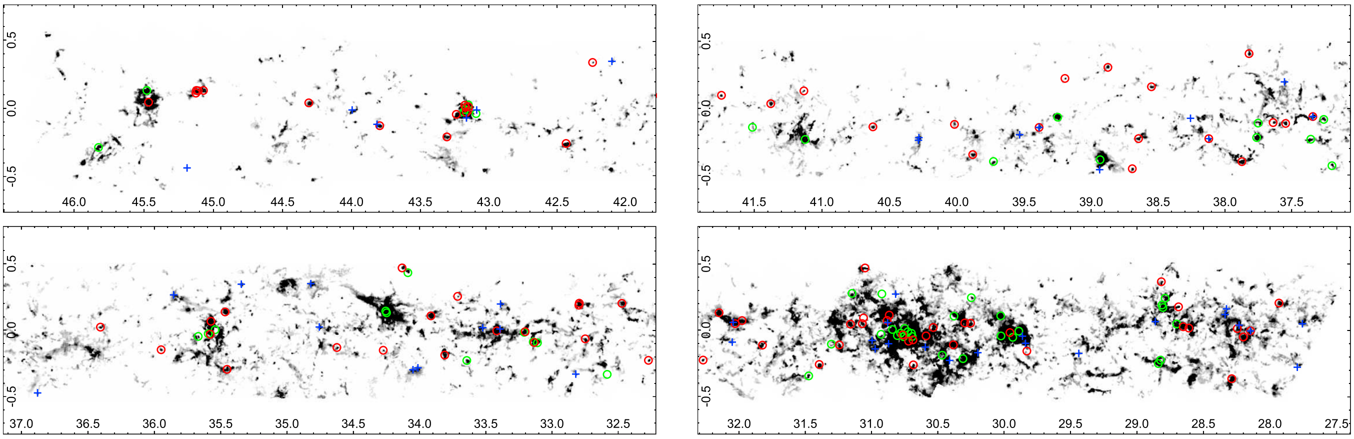

Fig. 1. Integrated ^{13}CO $J = 3-2$ emission maps of the whole region surveyed by the CHIMPS survey. All selected sources from the Red MSX Source Catalog (Lumsden et al. 2013) lying in this region are presented as follows: YSOs (blue crosses), HII regions (red circles), and diffuse HII regions (green circles).

Fich et al. (1989), obtaining a pair of possible distances to us (the nearest and farthest) due to the distance ambiguity in the first Galactic quadrant. Finally, using this pair of possible distances, we obtained the corresponding galactocentric distances, which in all cases are almost the same whether we used the nearest or farthest distances derived from the $v_{\rm LSR}^{18}$. Thus, no ambiguity in the galactocentric distances appears in the studied sources. Most of the sources are located at galactocentric distances between 4.0 and 6.5 kpc; taking into account the Galactic longitude range of the surveyed area, this indicates that we are mainly studying sources in the Scutum-Crux and Sagitarius-Carina Galactic arms.

We estimated the column densities of ^{13}CO and C^{18}O assuming that the rotational levels of these molecules are in local thermodynamic equilibrium (LTE). The optical depths ($\tau_{^{13}\rm CO}$ and $\tau_{\rm C^{18}O}$) and column densities ($N(^{13}$CO) and N(C^{18}O)) can be derived using the following equations:

$$\tau_{^{13}\rm CO} = -\ln\left(1 - \frac{T_{\rm mb}(^{13}\rm CO)}{15.87\left[\frac{1}{e^{15.87/T_{\rm ex}}-1} - 0.0028\right]}\right), \quad (1)$$

$$N(^{13}\rm CO) = 8.28\times10^{13}\, e^{\frac{15.85}{T_{\rm ex}}}\,\frac{T_{\rm ex}+0.88}{1-e^{\frac{-15.87}{T_{\rm ex}}}}\int \tau_{^{13}\rm CO}\,{\rm d}v, \quad (2)$$

with

$$\int \tau_{^{13}\rm CO}\,{\rm d}v = \frac{1}{J(T_{\rm ex})-0.044}\,\frac{\tau_{^{13}\rm CO}}{1-e^{-\tau_{^{13}\rm CO}}}\int T_{\rm mb}(^{13}\rm CO)\,{\rm d}v, \quad (3)$$

$$\tau_{\rm C^{18}O} = -\ln\left(1 - \frac{T_{\rm mb}(\rm C^{18}O)}{15.81\left[\frac{1}{e^{15.81/T_{\rm ex}}-1} - 0.0028\right]}\right), \quad (4)$$

$$N(\rm C^{18}O) = 8.26\times10^{13}\, e^{\frac{15.80}{T_{\rm ex}}}\,\frac{T_{\rm ex}+0.88}{1-e^{\frac{-15.81}{T_{\rm ex}}}}\int \tau_{\rm C^{18}O}\,{\rm d}v, \quad (5)$$

with

$$\int \tau_{\rm C^{18}O}\,{\rm d}v = \frac{1}{J(T_{\rm ex})-0.045}\,\frac{\tau_{\rm C^{18}O}}{1-e^{-\tau_{\rm C^{18}O}}}\int T_{\rm mb}(\rm C^{18}O)\,{\rm d}v. \quad (6)$$

The $J(T_{\rm ex})$ parameter is $\frac{15.87}{e^{\frac{15.87}{T_{\rm ex}}}-1}$ in the case of Eq. (3) and $\frac{15.81}{e^{\frac{15.81}{T_{\rm ex}}}-1}$ in Eq. (6). In all equations, $T_{\rm mb}$ is the peak main brightness temperature obtained from Gaussian fits (see Table A.1) and $T_{\rm ex}$ the excitation temperature. Assuming that the ^{12}CO $J = 3-2$ emission is optically thick, the $T_{\rm ex}$ was derived from

$$T_{\rm ex} = \frac{16.6}{\ln[1 + 16.6/(T_{\rm peak}(^{12}\rm CO) + 0.036)]}, \quad (7)$$

where $T_{\rm peak}(^{12}$CO) is the peak main brightness temperature obtained from the Gaussian fitting to the ^{12}CO $J = 3-2$ line. In cases where the ^{12}CO emission appears self-absorbed, the central component of the spectrum was corrected for absorption (see Fig. 2) in order to obtain a value for $T_{\rm peak}(^{12}$CO). In these cases, the best single Gaussian that fits the wings of the self-absorbed profile was used. This procedure was also applied in a few ^{13}CO spectra that presented signatures of self-absorption. It is important to note that the ^{13}CO and C^{18}O spectra were carefully inspected to look for signatures of saturation in the line which would generate an underestimation in some of its parameters. Besides the few cases of self-absorbed ^{13}CO emission already mentioned, we did not find any feature suggesting line saturation in the ^{13}CO and C^{18}O spectra. Line saturation is discussed in Sect. 4.1.

Table A.2 presents the results obtained for each source: the source number, type, galactocentric distance, and the integrated line ratio ($I^{13/18} = \int T_{\rm mb}^{13}\,{\rm d}v / \int T_{\rm mb}^{18}\,{\rm d}v$) are presented in Cols. 1, 2, 3, and 4, respectively, and the $T_{\rm ex}$, τ^{13}, $N(^{13}$CO), τ^{18}, N(C^{18}O), and the abundance ratio $X^{13/18}$ obtained from $N(^{13}$CO)/N(C^{18}O) are included in the others columns.

Figure 3 presents histograms of the number of sources vs. the abundance ratio ($X^{13/18}$) for YSOs, HII regions, and diffuse HII regions. The width of the histogram bar is 0.5, thus the height of the bar represents the number of sources that have abundance ratios distributed from the center of the bar ±0.25. Figure 4 shows the integrated line relation between the isotopes, i.e., $I^{13} = \int T_{\rm mb}^{13}\,{\rm d}v$ vs. $I^{18} = \int T_{\rm mb}^{18}\,{\rm d}v$.

Table 1 presents the mean values of the abundance and integrated line ratios ($\overline{X^{13/18}}$ and $\overline{I^{13/18}}$) for each kind of source together with the total number of sources composing each sample (N). The values in parentheses are the results obtained after removing the outlier points of each sample (see the bars totally detached from the main distribution in Fig. 3).

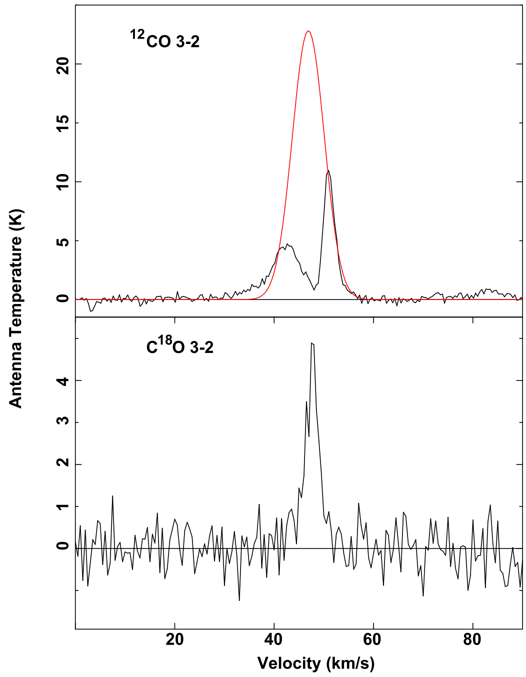

Fig. 2. Example of a ^{12}CO self-absorption correction. The C^{18}O emission peaks at the ^{12}CO dip, showing that the ^{12}CO emission is self-absorbed. The Gaussian fit to the central component corrected for absorption is shown.

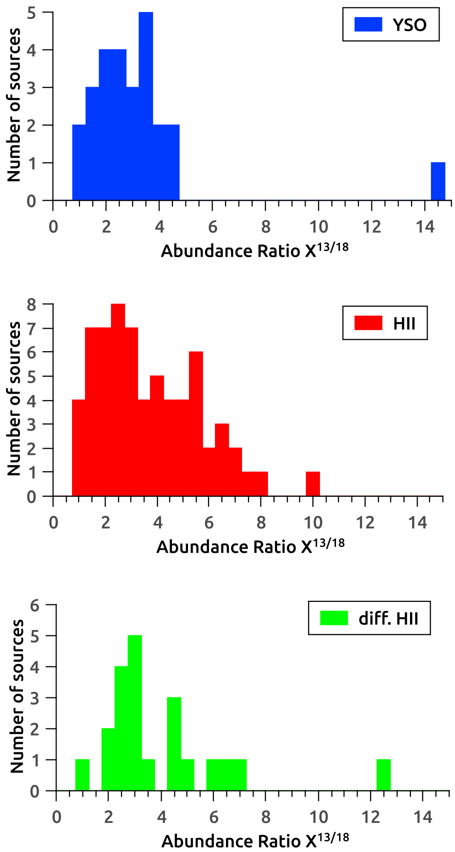

Fig. 3. Number of sources vs. the ^{13}CO/C^{18}O abundance ratio ($X^{13/18}$).

Figure 5 displays the obtained abundance ratio for each source vs. the C^{18}O column density. Figure 6 displays the abundance ratio $X^{13/18}$ vs. the integrated line ratio $I^{13/18}$, which shows good linear relations. The results from linear fittings for each kind of source are presented in Table 2. The χ^2 factor obtained from each fitting is also included. As in Table 1, the results obtained after removing the above mentioned outlier points are shown in parentheses. These points are $(X^{13/18}, I^{13/18}) = (14.3, 10.8)$ for a YSO, (9.8, 10.5) for a HII region, and (12.7, 12.3) for a diffuse HII region.

Table 1. Mean values of the abundance and integrated line ratios.

	N	$\overline{X^{13/18}}$	$\overline{I^{13/18}}$
YSO	26	3.13 (2.68)	3.27 (2.97)
HII	67	3.68 (3.59)	3.65 (3.55)
diffuse HII	21	4.09 (3.66)	4.36 (3.96)

Notes. Values between parentheses are the results obtained after removing the outlier points of each sample.

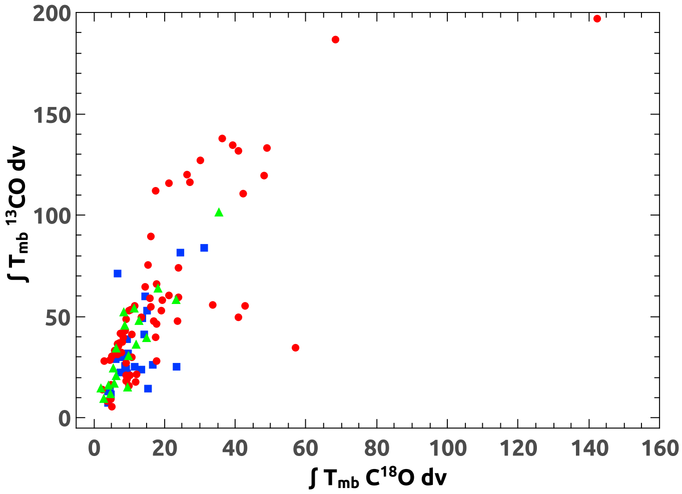

Fig. 4. Integrated ^{13}CO line vs. the integrated C^{18}O line. YSOs, HII regions, and diffuse HII regions are represented with blue squares, red circles, and green triangles, respectively.

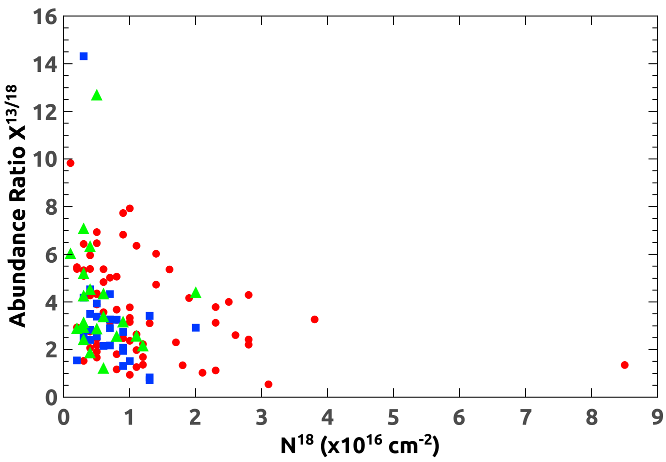

Fig. 5. Abundance ratio vs. C^{18}O column density. YSOs, HII regions, and diffuse HII regions are represented with blue squares, red circles, and green triangles, respectively.

Table 2. Linear fitting results ($A\,x + B$) from the data presented in Fig. 6.

	A	B	χ^2
YSO	1.33 ± 0.05 (0.98 ± 0.04)	−1.24 ± 0.19 (−0.25 ± 0.15)	0.96 (0.94)
HII	1.05 ± 0.05 (1.10 ± 0.05)	−0.17 ± 0.20 (−0.32 ± 0.22)	0.87 (0.84)
Diffuse HII	1.04 ± 0.04 (0.97 ± 0.07)	−0.43 ± 0.24 (−0.20 ± 0.30)	0.95 (0.89)

Notes. Values between parentheses are the results obtained after removing the outlier points of each sample.

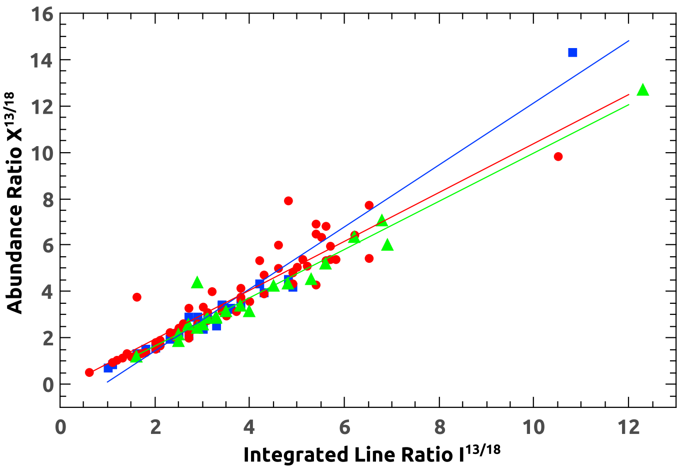

Fig. 6. Abundance ratio $X^{13/18}$ vs. integrated line ratio $I^{13/18}$. YSOs, HII regions, and diffuse HII regions are represented with blue squares, red circles, and green triangles, respectively. Linear fittings to each set of data for the whole sample are displayed.

4. Discussion

Taking into account that the molecular gas related to YSOs should be less affected by the UV radiation than the gas associated with HII regions, as a first result of the analysis of the ^{13}CO/C^{18}O abundance ratios $X^{13/18}$ obtained towards the 114 studied sources, it can be suggested that $X^{13/18}$ increases as the degree of UV radiation increases. It is important to note that it is likely that the molecular gas related to some sources catalogued as YSOs can be affected by the UV radiation. These sources could be located at the borders of extended HII regions and/or they may be transiting the last stages of star formation and have begun to ionize their surroundings. However, we consider that the gas associated with most of them should be less affected by the radiation than in the case of sources catalogued as HII and diffuse HII regions. This phenomenon is indeed reflected in our analysis. Figure 3 shows that YSOs tend to have smaller $X^{13/18}$ values than the other type of sources, which can also be appreciated by comparing the mean values presented in Table 1. This result is in agreement with what it is observed in different regions of molecular clouds that are affected by far-UV radiation, such as the Orion-A giant molecular cloud (Shimajiri et al. 2014), and what it is predicted from photodissociation models (Visser et al. 2009; van Dishoeck & Black 1988). Thus, we confirm, through a large sample of sources, that selective far-UV photodissociation of C^{18}O indeed occurs. Moreover, as Fig. 5 shows, the $X^{13/18}$ ratio decreases with increasing C^{18}O column density in all sources, which suggests that this phenomenon occurs even considering each group of sources separately.

The relation between the isotopes integrated line (I^{13} vs. I^{18}, see Fig. 4) shows slight differences between the kind of source. This is also reflected in the relation between the abundance and the integrated line ratios (Fig. 6), which is an interesting relation because it compares values that were derived from excitation considerations (LTE assumption) with values that are direct measurements. These relations show that the ^{13}CO/C^{18}O abundance ratio can be estimated directly from the integrated line ratios, as can be seen by comparing the values presented in Table 1.

4.1. Saturation of the $J = 3-2$ line

It is known that a linear molecule may increase its opacity with the increase in the J rotational level until reaching a maximum J ($J_{\rm max}$) for which the optical depth exhibits a peak (Goldsmith & Langer 1999). The $J_{\rm max}$ depends on the temperature and the molecule rotational constant. Thus, depending on the temperature of the region, it is possible that the CO $J = 3-2$ line can suffer more saturation than the lower transitions, and hence a quantitative comparison of the abundance ratio with previous results obtained from the $J = 2-1$ and $1-0$ lines should be done with caution.

Wouterloot et al. (2008) measured the ^{13}CO/C^{18}O integrated intensity ratio ($I^{13/18}$) using the $J = 1-0$ and $J = 2-1$ line towards some Galactic star forming and HII regions, and suggested that saturation can be more pronounced in the $J = 2-1$ transition. We compare our ^{13}CO/C^{18}O integrated intensity ratios with those obtained by Wouterloot et al. (2008 see their Fig. 3) in the galactocentric distance range (4–8 kpc). We find that they do not present large discrepancies. Our results are very similar to those obtained from the $J = 2-1$ line in Wouterloot et al. (2008), suggesting that the saturation does not increase considerably from $J = 2-1$ to $J = 3-2$ in this kind of source, and moreover, in some cases it is comparable even with the value obtained from the $J = 1-0$ line.

Thus, taking into account that the ^{13}CO and C^{18}O spectra do not present any signature of line saturation, that almost all τ^{13} and all τ^{18} values are lower than unity (see Table A.2), and that our ^{13}CO/C^{18}O integrated intensity ratios are in good agreement with those obtained from the $J = 2-1$ and $1-0$ lines in a previous work towards similar sources, we conclude that line saturation should not be an important issue in our analysis.

4.2. Abundance ratio and the distance

Given that the elemental abundance ratios ^{12}C/^{13}C and ^{16}O/^{18}O, among others, presented in Wilson & Rood (1994) are largely used in the literature when CO data are studied, we compared our results with theirs. The abundance relations presented in Wilson & Rood (1994) are

$$(^{12}\mathrm{C}/^{13}\mathrm{C}) = (7.5 \pm 1.9) \times D_{\rm GC} + (7.6 \pm 12.9), \tag{8}$$

$$(^{16}\mathrm{O}/^{18}\mathrm{O}) = (58.8 \pm 11.8) \times D_{\rm GC} + (37.1 \pm 82.6), i \tag{9}$$

where $D_{\rm GC}$ is the galactocentric distance. Thus, to assume a ^{13}CO/C^{18}O abundance ratio it is necessary to perform a double

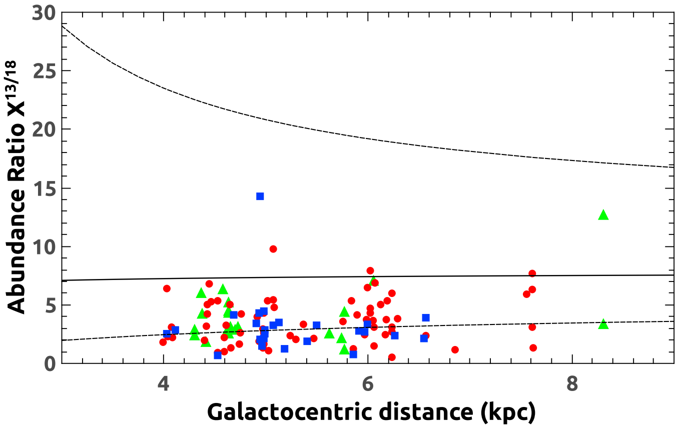

Fig. 7. Abundance ratio $X^{13/18}$ vs. galactocentric distance. The continuous black curve is the plot of the ^{13}CO/C^{18}O abundance ratio from Wilson & Rood (1994) (Eq. (10)). Dashed curves are the result of plotting this equation considering the errors bars.

ratio between the above expressions, yielding

$$\frac{^{13}\mathrm{CO}}{\mathrm{C}^{18}\mathrm{O}} = \frac{(58.8 \pm 11.8) \times D_{\mathrm{GC}} + (37.1 \pm 82.6)}{(7.5 \pm 1.9) \times D_{\mathrm{GC}} + (7.6 \pm 12.9)}. \tag{10}$$

Figure 7 displays the abundance ratio $X^{13/18}$ vs. galactocentric distance for the sources analyzed in this work. The black curve is the plot of Eq. (10), which shows that the mean value of the $X^{13/18}$ ratio is between 7 and 8 for the whole galactocentric distance range. The dashed curves are the result of plotting this equation considering the errors bars. These curves delimit a region where, according to Wilson & Rood (1994), the sources should lie.

The analyzed sources lie mainly in the galactocentric distance range 4.0–6.5 kpc, and a few have greater distances, around 8 kpc. Thus, our analysis lacks information concerning the molecular gas lying within a radius of 4 kpc from the Galactic center. Figure 7 shows that almost all the abundance ratio values of our complete sample are lower than the mean value predicted by Wilson & Rood (1994) and, moreover, that there are many values lying under the lower limit from Eq. (10) (bottom dashed curve in Fig. 7). This suggests that the ^{13}CO/C^{18}O abundance ratio derived from the double ratio between ^{12}C/^{13}C and ^{16}O/^{18}O could overestimate the actual value.

5. Summary and concluding remarks

Using the ^{12}CO, ^{13}CO, and C^{18}O $J = 3-2$ emission obtained from the COHRS and CHIMPS surveys performed with the JCMT telescope and using additional data from the telescope database, we studied the ^{13}CO/C^{18}O abundance ratio towards a large sample of YSOs and HII regions located in the first Galactic quadrant.

From the statistical analysis of the $X^{13/18}$ ratio we found that YSOs have, on average, smaller values than HII and diffuse HII regions. Taking into account that the gas associated with YSOs should be less affected by the radiation than in the case of HII and diffuse HII regions, we can confirm the selective far-UV photodissociation of C^{18}O as it was observed in previous works towards particular molecular clouds and as it was predicted by models. Additionally, we find a linear relation between the abundance ratios and the integrated line ratios ($I^{13/18}$), suggesting that the ^{13}CO/C^{18}O abundance ratio can be estimated directly from $I^{13/18}$.

Most of the sources are located in the galactocentric distance range 4.0–6.5 kpc, which indicates that we are mainly studying sources in the Scutum-Crux and Sagitarius-Carina Galactic arms. A few sources are located as far away as 8 kpc. Thus, our analysis does not include information concerning the molecular gas lying within a radius of 4 kpc from the Galactic center. Extension of the used surveys or other ^{12}CO, ^{13}CO, and C^{18}O surveys covering the inner Galaxy would be useful to complete this study. From the galactocentric distance range covered, it was shown that the ^{13}CO/C^{18}O abundance ratios obtained directly from the molecular emission are lower than if they are derived from the known elemental abundances relations.

Finally, it is important to mention that this is the first ^{13}CO/C^{18}O abundance ratio study obtained directly from CO observations towards a large sample of sources of different natures at different locations. Thus, the ^{13}CO/C^{18}O abundance ratios derived in this work will be useful for future studies of molecular gas associated with YSOs and HII regions based on the observation of these isotopes.

Acknowledgements. We thank the anonymous referee for her/his helpful comments and suggestions. M.B.A. and M.C.P. are doctoral fellows of CONICET, Argentina. S.P. and M.O. are members of the Carrera del Investigador Científico of CONICET, Argentina. This work was partially supported by Argentina grants awarded by UBA (UBACyT), CONICET, and ANPCYT.

References

Buckle, J. V., Hills, R. E., Smith, H., et al. 2009, MNRAS, 399, 1026
Currie, M. J., Berry, D. S., Jenness, T., et al. 2014, in Astronomical Data Analysis Software and Systems XXIII, eds. N. Manset, & P. Forshay, ASP Conf. Ser., 485, 391
Dempsey, J. T., Thomas, H. S., & Currie, M. J. 2013, ApJS, 209, 8
Dickman, R. L., McCutcheon, W. H., & Shuter, W. L. H. 1979, ApJ, 234, 100
Fich, M., Blitz, L., & Stark, A. A. 1989, ApJ, 342, 272
Goldsmith, P. F., & Langer, W. D. 1999, ApJ, 517, 209
Kong, S., Lada, C. J., Lada, E. A., et al. 2015, ApJ, 805, 58
Langer, W. D., Goldsmith, P. F., Carlson, E. R., & Wilson, R. W. 1980, ApJ, 235, L39
Lin, S.-J., Shimajiri, Y., Hara, C., et al. 2016, ApJ, 826, 193
Lumsden, S. L., Hoare, M. G., Urquhart, J. S., et al. 2013, ApJS, 208, 11
Milam, S. N., Savage, C., Brewster, M. A., Ziurys, L. M., & Wyckoff, S. 2005, ApJ, 634, 1126
Rigby, A. J., Moore, T. J. T., Plume, R., et al. 2016, MNRAS, 456, 2885
Shimajiri, Y., Kitamura, Y., Saito, M., et al. 2014, A&A, 564, A68
Szűcs, L., Glover, S. C. O., & Klessen, R. S. 2014, MNRAS, 445, 4055
van Dishoeck, E. F., & Black, J. H. 1988, ApJ, 334, 771
Visser, R., van Dishoeck, E. F., & Black, J. H. 2009, A&A, 503, 323
Wilson, T. L. 1999, Rep. Prog. Phys., 62, 143
Wilson, T. L., & Rood, R. 1994, ARA&A, 32, 191
Wouterloot, J. G. A., Henkel, C., Brand, J., & Davis, G. R. 2008, A&A, 487, 237

Appendix A

Table A.1. Line parameters for the CO isotopes.

#	Source	Type	D_{gal} (kpc)	v^{12}_{LSR} (km s^{-1})	Δv^{12} (km s^{-1})	T^{12}_{mb} (K)	v^{13}_{LSR} (km s^{-1})	Δv^{13} (km s^{-1})	T^{13}_{mb} (K)	$\int T^{13}_{mb}\,dv$ (K km s^{-1})	v^{18}_{LSR} (km s^{-1})	Δv^{18} (km s^{-1})	T^{18}_{mb} (K)	$\int T^{18}_{mb}\,dv$ (K km s^{-1})
1	G027.7954–00.2772	YSO	6.0	45.2	6.6	5.7	46.6	3.6	6.1	25.4	46.6	2.6	3.1	8.7
2	G027.9334+00.2056	HII	4.0	43.7	7.5	6.6	42.3	2.7	5.7	18.3	42.6	2.8	3.2	8.9
3	G028.1467–00.0040A	YSO	4.5	96.5	10.9	7.9	97.7	1.4	4.2	14.6	98.8	2.9	4.7	15.1
4	G028.1467–00.0040B	HII	4.5	96.1	6.8	3.4	98.3	1.7	3.3	5.7	98.7	1.2	3.1	5.0
5	G028.2007–00.0494A	HII	4.6	96.5	16.3	20.3	96.2	13.2	6.3	96.0	98.0	3.6	8.3	48.8
6	G028.2007–00.0494B	HII	4.6	96.5	15.0	23.3	94.4	5.1	7.5	50.0	95.9	6.6	5.6	40.8
7	G028.2325+00.0394	YSO	4.0	105.5	14.5	8.7	107.1	4.6	2.1	13.1	106.7	2.4	2.2	3.9
8	G028.2461+00.0134	HII	4.0	104.5	5.5	15.0	105.5	2.7	10.4	30.7	107.0	3.4	1.4	4.9
9	G028.2875–00.3639	HII	4.0	48.0	7.9	73.8	47.5	7.3	6.6	59.7	47.7	3.4	5.9	23.8
10	G028.3271+00.1617	YSO	5.0	24.4	8.3	8.8	25.7	4.3	5.2	24.3	25.3	4.4	2.9	13.4
11	G028.3373+00.1189	YSO	4.9	79.6	11.6	6.3	81.2	5.7	4.2	24.6	80.8	2.3	4.4	9.0
12	G028.6096+00.0170	HII	4.1	101.2	2.4	20.7	103.2	4.8	12.5	74.2	102.8	4.3	5.1	23.9
13	G028.6520+00.0271	HII	4.1	103.2	8.2	9.6	103.4	4.0	8.5	40.1	104.1	5.3	3.0	17.4
14	G028.6874+00.1772	HII	4.5	83.5	4.2	17.8	84.1	3.7	9.1	42.1	84.0	3.2	2.7	7.4
15	G028.7014+00.0478	diffuse HII	4.4	100.1	8.9	19.0	99.9	2.1	5.9	14.7	99.6	1.1	2.0	2.1
16	G028.8392–00.2507	diffuse HII	4.6	89.2	9.6	28.5	89.1	3.3	8.2	30.6	87.1	2.4	3.7	9.7
17	G028.8621+00.0657	YSO	4.1	104.8	7.1	15.2	103.9	4.8	15.2	84.0	103.0	3.3	8.3	31.0
18	G029.8620–00.0444	YSO	4.9	99.8	8.4	31.2	101.4	5.2	14.8	81.7	101.0	3.0	7.3	24.3
19	G029.9564–00.0174	HII	4.9	96.3	8.9	45.0	97.3	5.5	22.0	132.2	97.5	4.0	9.6	40.8
20	G030.0240–00.0427	diffuse HII	4.6	92.9	6.1	34.6	93.3	4.0	11.5	52.2	92.8	3.0	2.5	8.5
21	G030.0261+00.1088	diffuse HII	4.3	106.0	5.1	14.1	105.1	3.0	5.2	17.1	105.5	2.1	2.7	5.9
22	G030.1981–00.1691	YSO	4.9	103.5	8.2	30.4	103.1	4.3	12.9	60.3	102.5	3.0	4.3	14.3
23	G030.2531+00.0536	HII	4.7	70.1	6.1	13.8	71.3	4.6	4.1	19.4	70.2	3.6	2.5	9.4
24	G030.2971+00.0549	HII	4.9	107.2	4.3	24.5	108.1	2.5	8.2	21.4	107.5	2.3	4.1	10.1
25	G030.3101–00.2142	diffuse HII	4.4	101.8	4.1	20.1	102.4	2.2	9.8	24.7	103.2	1.6	3.9	5.5
26	G030.3782+00.1068	diffuse HII	4.3	109.6	3.1	13.2	110.4	1.5	5.7	9.4	110.1	1.3	2.0	2.8
27	G030.3830–00.1099	HII	4.8	86.1	2.4	2.6	86.5	3.2	14.4	48.9	86.6	2.2	3.4	9.1
28	G030.4117–00.2277	YSO	4.9	103.9	4.1	20.1	104.7	3.8	17.4	71.3	105.2	2.1	3.1	6.6
29	G030.5345+00.0209	HII	4.4	47.1	6.7	39.4	48.3	4.6	18.5	89.9	47.8	4.0	4.0	16.1
30	G030.5889–00.0426	HII	4.4	42.8	4.9	12.1	42.0	9.2	4.6	46.8	41.7	2.9	5.6	17.5
31	G030.5942–00.1273	YSO	5.0	83.4	4.8	14.3	84.7	3.0	2.5	7.9	84.7	1.5	2.4	4.0
32	G030.6848–00.2613	HII	5.0	103.0	6.9	23.5	102.8	5.5	10.3	60.6	103.5	3.6	5.6	21.1
33	G030.6877–00.0729	HII	5.0	92.0	10.2	23.6	94.8	8.5	5.4	48.2	92.0	4.1	4.8	23.5
34	G030.6931–00.0474	diffuse HII	4.7	91.2	11.6	34.4	88.9	7.5	6.0	63.9	89.4	5.6	3.2	18.1
35	G030.7206–00.0826	HII	5.0	92.9	10.9	28.3	92.4	8.6	6.1	56.1	93.0	4.2	7.3	33.6
36	G030.7498+00.0134	diffuse HII	4.6	93.1	6.8	6.2	93.0	12.3	3.5	36.1	92.7	8.2	1.4	12.0
37	G030.7581–00.0487	diffuse HII	4.6	93.6	12.3	23.7	93.4	13.0	3.4	45.8	92.7	7.8	1.2	8.6

Notes. The superscripts 12, 13, and 18 mean ^{12}CO, ^{13}CO, and $C^{18}O$, respectively. In the case of ^{12}CO and ^{13}CO, the typical errors (the formal 1σ value for the model of the Gaussian line shape) in T_{mb} are between 5% and 10%, while the typical error in this parameter for $C^{18}O$ ranges from 10% to 20%. The integrated line emission has typical errors of 5–10 % and 10–20% for ^{13}CO and $C^{18}O$, respectively.

Table A.1. continued.

#	Source	Type	D_{gal} (kpc)	v_{LSR}^{12} (km s^{-1})	Δv^{12} (km s^{-1})	T_{mb}^{12} (K)	v_{LSR}^{13} (km s^{-1})	Δv^{13} (km s^{-1})	T_{mb}^{13} (K)	$\int T_{mb}^{13}\,dv$ (K km s^{-1})	v_{LSR}^{18} (km s^{-1})	Δv^{18} (km s^{-1})	T_{mb}^{18} (K)	$\int T_{mb}^{18}\,dv$ (K km s^{-1})
38	G030.7653–00.0352C	HII	5.0	82.1	6.1	17.9	81.0	3.4	4.6	16.5	80.7	3.2	1.9	4.8
39	G030.7808–00.0222	diffuse HII	4.6	93.1	6.1	18.0	93.0	4.9	6.7	34.3	91.9	3.6	1.6	6.2
40	G030.8053–00.0403	diffuse HII	4.6	91.5	11.3	16.9	92.8	6.6	7.7	54.2	93.0	4.5	2.3	11.4
41	G030.8185+00.2729	YSO	5.0	98.0	10.5	9.7	98.6	3.9	6.9	29.3	98.0	3.9	1.5	6.1
42	G030.8667+00.1141	HII	4.4	38.7	8.7	26.8	39.1	6.0	11.8	75.8	39.3	4.3	3.4	15.1
43	G030.8786+00.0566	YSO	5.0	75.7	5.5	8.0	76.1	3.0	7.0	22.1	75.3	2.3	3.6	9.2
44	G030.9726-00.1410	YSO	5.0	77.9	5.5	14.3	77.8	3.6	6.5	25.8	77.4	2.2	3.6	8.6
45	G030.9959–00.0771	YSO	5.0	81.1	4.2	28.0	81.2	2.9	13.2	41.4	81.5	2.1	6.2	14.2
46	G031.0494+00.4698	HII	4.4	33.0	7.1	13.1	33.8	4.3	6.8	31.4	33.6	1.8	2.5	6.5
47	G031.0702+00.0498	HII	4.5	37.5	5.7	19.8	38.3	3.6	8.4	33.3	38.0	3.8	1.5	5.9
48	G031.1475+00.2780	diffuse HII	4.4	103.0	11.5	6.9	103.2	5.3	1.9	11.8	103.5	2.1	2.2	4.8
49	G031.2430–00.1108	HII	4.4	19.8	8.4	25.9	20.5	4.8	9.8	54.9	20.8	3.6	3.9	16.0
50	G031.3948–00.2585	HII	5.0	88.0	5.7	36.2	87.4	5.5	20.4	127.5	86.8	4.7	6.4	30.1
51	G031.4134+00.3092	HII	5.0	96.0	9.5	27.0	97.4	5.4	9.8	55.6	97.6	5.3	7.7	42.6
52	G031.4743–00.3452	diffuse HII	4.7	92.0	3.9	24.6	91.3	3.1	6.3	20.8	91.3	3.1	2.0	6.4
53	G031.8237–00.1131	HII	4.6	39.1	4.1	23.6	40.3	3.3	10.3	35.7	39.4	2.3	2.7	6.9
54	G032.0301+00.0495	HII	5.1	95.0	7.4	17.0	95.8	5.5	4.9	29.0	96.3	1.3	2.5	4.5
55	G032.0451+00.0589	YSO	5.1	94.0	12.3	23.3	95.4	4.9	8.7	49.2	95.3	3.1	4.1	13.6
56	G032.1514+00.1317	HII	5.1	94.2	5.1	27.6	96.0	5.1	10.3	55.6	95.1	3.2	3.0	11.3
57	G032.4727+00.2041	HII	5.0	50.1	10.9	15.5	49.4	5.8	6.9	43.1	49.0	3.9	2.2	8.8
58	G032.7977+00.1903	HII	4.6	16.0	9.1	23.7	14.1	9.6	18.8	186.8	14.9	7.6	8.4	68.3
59	G033.1342–00.0915	HII	5.2	75.5	9.5	22.1	75.7	7.8	6.6	53.1	76.4	3.9	4.7	18.9
60	G033.2031–00.0102	HII	4.7	98.8	5.4	6.7	98.5	4.5	4.9	21.9	99.3	2.0	5.4	12.0
61	G033.2101–00.0148	diffuse HII	4.7	99.9	3.4	10.2	100.1	3.8	4.0	16.3	100.1	1.1	2.9	4.1
62	G033.3891+00.1989	YSO	5.1	84.2	4.7	17.2	84.6	3.0	9.1	30.3	85.0	1.9	4.1	7.9
63	G033.3933+00.0100	YSO	4.7	103.1	8.9	20.2	103.0	5.7	5.5	32.4	103.4	2.3	3.1	6.5
64	G033.4178–00.0038	HII	5.3	73.1	5.3	22.4	74.1	3.7	5.4	21.5	73.9	5.2	1.7	9.1
65	G033.6437–00.2277	diffuse HII	5.6	60.1	5.2	14.2	60.8	3.6	10.0	39.4	61.7	3.8	3.7	14.9
66	G033.9148+00.1093	HII	4.7	106.7	7.0	36.2	107.9	4.3	18.0	110.7	107.9	3.0	12.8	42.1
67	G034.2496+00.1322	diffuse HII	5.8	57.0	6.0	9.6	58.4	7.0	2.0	15.4	58.0	4.3	2.1	9.6
68	G034.2557+00.1454	diffuse HII	5.8	57.4	6.8	26.6	57.5	3.8	23.0	101.3	58.1	4.2	8.1	35.4
69	G034.2746–00.1507	HII	6.2	48.3	14.2	2.9	49.0	2.3	6.8	16.1	49.1	2.4	2.7	9.8
70	G034.6243–00.1300	HII	5.1	23.1	5.4	17.0	23.1	3.0	8.2	28.5	23.6	1.2	1.8	2.7
71	G034.7569+00.0247	YSO	5.4	75.1	6.3	8.4	76.1	3.3	7.3	25.6	76.1	1.8	4.8	11.3
72	G035.4524–00.2950	HII	6.0	53.7	18.0	5.1	54.8	3.6	9.8	37.9	55.3	2.0	4.3	7.9
73	G035.4672+00.1381	HII	5.4	76.1	2.9	28.5	76.5	3.2	17.0	58.1	77.8	2.5	7.3	19.3
74	G035.5736+00.0678	HII	6.0	48.6	9.6	23.8	48.5	4.7	11.7	59.2	49.9	2.9	4.8	15.7
75	G035.5789–00.0304	HII	6.0	51.1	8.5	35.5	52.0	7.1	15.6	116.7	52.8	4.9	5.1	26.9
76	G036.4057+00.0230	HII	6.0	58.0	5.4	16.2	57.3	5.2	11.6	66.4	56.8	3.7	4.2	17.6
77	G037.3412–00.0600A	YSO	6.0	54.7	3.6	31.3	54.6	2.4	12.2	32.2	55.5	2.0	4.4	9.5
78	G037.3412–00.0600B	HII	6.0	54.5	4.2	23.4	54.5	2.9	16.9	53.3	55.3	2.1	4.4	9.9
79	G037.5450–00.1118	HII	6.1	50.8	5.6	39.6	51.6	4.3	14.8	65.1	52.7	3.8	3.5	14.3

Table A.1. continued.

#	Source	Type	D_{gal} (kpc)	v^{12}_{LSR} (km s^{-1})	Δv^{12} (km s^{-1})	T^{12}_{mb} (K)	v^{13}_{LSR} (km s^{-1})	Δv^{13} (km s^{-1})	T^{13}_{mb} (K)	$\int T^{13}_{mb}\, dv$ (K km s^{-1})	v^{18}_{LSR} (km s^{-1})	Δv^{18} (km s^{-1})	T^{18}_{mb} (K)	$\int T^{18}_{mb}\, dv$ (K km s^{-1})
80	G037.5536+00.2008	YSO	5.2	85.0	7.0	19.6	85.7	3.5	5.5	26.4	84.4	4.2	4.1	16.5
81	G037.6390–00.1054	HII	6.3	44.0	4.7	12.1	45.6	3.7	8.2	32.4	46.4	2.3	3.4	7.6
82	G037.7625–00.2181	diffuse HII	5.7	65.0	9.5	22.2	64.1	7.5	7.5	58.2	63.3	4.6	4.7	23.3
83	G037.8195+00.4132	HII	6.0	17.7	7.6	17.8	15.7	6.5	7.1	48.1	16.8	4.4	3.6	16.8
84	G037.8730–00.3991	HII	5.9	60.1	17.2	26.4	61.1	8.2	15.3	138.1	61.1	6.2	5.2	36.3
85	G038.6462–00.2260	HII	5.8	68.1	4.0	21.9	69.7	4.0	9.9	41.5	68.5	1.8	5.8	10.5
86	G038.6930–00.4522	HII	6.2	51.0	3.9	17.0	51.0	4.1	12.4	53.5	50.6	2.9	3.6	10.4
87	G038.9365–00.4592	YSO	6.6	41.2	5.2	22.1	41.5	3.4	10.4	39.3	41.5	1.7	5.4	9.2
88	G039.3880–00.1421A	HII	5.9	65.2	7.0	11.8	65.0	4.4	5.9	28.5	65.7	3.1	5.2	17.5
89	G039.3880–00.1421B	YSO	5.9	66.6	8.2	18.2	66.5	4.4	5.4	25.3	65.2	3.3	6.3	23.3
90	G039.5328–00.1969	YSO	6.3	49.5	6.4	7.1	50.6	6.3	2.2	13.6	51.5	2.4	1.4	4.5
91	G039.8821–00.3457	HII	6.0	55.8	3.4	13.2	56.9	5.8	6.4	40.0	57.6	3.6	2.1	8.2
92	G040.0175–00.1193	HII	5.5	82.4	4.5	4.2	83.9	2.5	3.1	8.6	84.1	1.9	1.3	3.5
93	G040.2816–00.2190	YSO	5.5	71.2	17.0	19.7	71.5	4.1	8.8	53.3	70.5	4.0	3.6	15.0
94	G040.6225–00.1377	HII	6.9	32.6	14.2	10.2	32.7	4.7	3.6	17.9	32.7	3.5	3.1	11.8
95	G041.1331+00.1307	HII	6.1	59.6	4.4	9.0	61.6	4.3	2.1	9.4	60.4	1.8	2.0	4.6
96	G041.3780+00.0350	HII	6.1	58.6	6.2	8.8	59.1	2.9	11.7	37.4	58.7	2.7	2.4	7.0
97	G041.7410+00.0972	HII	7.6	12.6	5.5	9.0	12.8	3.7	9.0	36.7	13.6	3.1	1.9	6.5
98	G042.2396+00.3434	HII	5.8	–39.4	5.8	6.0	–40.2	2.7	4.7	14.0	–38.6	2.1	1.2	2.4
99	G043.1492+00.0130A	HII	7.6	9.3	9.5	41.1	9.8	6.5	16.4	115.8	8.8	5.8	3.2	21.1
100	G043.1492+00.0130B	HII	7.6	11.6	9.0	35.9	11.8	5.9	17.2	112.4	11.3	4.9	3.3	17.4
101	G043.1497+00.0272	diffuse HII	8.3	3.6	11.5	24.2	3.8	1.9	6.2	47.9	2.3	7.6	1.6	12.8
102	G043.1650–00.0285	HII	7.6	14.6	13.9	37.9	14.3	10.8	12.2	135.0	15.4	3.9	9.5	39.2
103	G043.1679+00.0095	HII	7.6	7.6	4.5	37.0	7.3	12.4	15.8	197.2	5.3	5.3	10.8	142.3
104	G043.1737–00.0074	diffuse HII	8.3	2.6	8.8	38.2	3.3	9.1	11.8	116.4	2.3	2.7	2.8	9.5
105	G043.3061–00.2106	HII	6.2	58.0	6.5	18.2	58.3	4.3	6.5	30.4	54.5	2.8	3.6	10.6
106	G043.7955–00.1275	HII	6.6	44.6	10.3	18.1	44.3	8.2	13.7	119.9	44.5	5.3	8.2	47.9
107	G043.8152–00.1172	YSO	6.5	47.0	3.5	4.4	46.8	3.2	3.3	11.7	47.0	2.1	1.8	4.8
108	G043.9956–00.0111	YSO	5.9	65.5	4.4	28.3	64.7	2.4	7.8	22.6	65.6	3.0	3.0	7.4
109	G044.3103+00.0416	HII	6.2	56.6	4.1	14.2	58.2	7.5	6.0	50.0	56.8	4.3	2.9	13.4
110	G045.0711+00.1325	HII	6.2	59.6	5.5	34.2	60.1	3.9	9.4	34.7	59.8	7.6	6.9	56.8
111	G045.1086+00.1302	HII	6.2	57.2	6.9	24.6	59.1	3.4	7.7	27.2	58.6	2.5	3.3	8.9
112	G045.1221+00.1323	HII	6.2	59.6	8.3	40.1	59.6	5.1	21.0	120.3	60.3	4.1	5.4	26.1
113	G045.4658+00.0457	HII	6.1	60.7	8.1	17.6	61.3	0.4	9.8	66.9	62.2	3.9	4.7	19.4
114	G045.4782+00.1323	diffuse HII	6.1	61.4	3.5	30.6	61.8	3.6	11.6	47.9	62.7	3.6	1.7	7.1

Table A.2. Results.

#	Type	D_{gal} (kpc)	$I^{13/18}$	T_{ex} (K)	τ^{13}	N^{13} ($\times 10^{16}$ cm^{-2})	τ^{18}	N^{18} ($\times 10^{16}$ cm^{-2})	$X^{13/18}$
1	YSO	6.0	2.9	12.3	0.7	2.5	0.3	0.9	2.8
2	HII	4.0	2.0	13.2	0.6	1.5	0.3	0.8	1.8
3	YSO	4.5	1.0	14.7	0.3	0.9	0.4	1.3	0.7
4	HII	4.5	1.1	9.5	0.5	0.9	0.5	1.0	1.0
5	HII	4.6	2.7	27.8	0.4	6.2	0.4	2.8	2.2
6	HII	4.6	1.2	30.9	0.3	2.2	0.2	2.1	1.0
7	YSO	4.0	3.3	15.6	0.1	0.7	0.1	0.3	2.6
8	HII	4.0	6.2	22.3	0.7	1.7	0.1	0.3	6.4
9	HII	4.0	2.5	81.8	0.2	3.8	0.2	1.7	2.3
10	YSO	5.0	1.8	15.7	0.4	1.5	0.2	1.0	1.5
11	YSO	4.9	2.7	12.9	0.4	2.0	0.4	0.9	2.1
12	HII	4.1	3.1	28.2	0.7	3.9	0.2	1.3	3.1
13	HII	4.1	2.3	16.5	0.7	2.7	0.2	1.2	2.2
14	HII	4.5	5.7	25.3	0.5	2.0	0.1	0.4	5.4
15	diffuse HII	4.4	6.9	26.5	0.3	0.6	0.1	0.1	6.0
16	diffuse HII	4.6	3.1	36.2	0.3	1.4	0.1	0.5	2.9
17	YSO	4.1	2.7	22.5	1.3	5.8	0.5	2.0	2.9
18	YSO	4.9	3.4	38.9	0.7	4.5	0.3	1.3	3.4
19	HII	4.9	3.2	53.0	1.2	10.0	0.4	2.5	4.0
20	diffuse HII	4.6	6.2	42.4	0.5	2.7	0.1	0.4	6.3
21	diffuse HII	4.3	2.9	21.4	0.3	0.8	0.1	0.3	2.4
22	YSO	4.9	4.2	38.1	0.6	3.1	0.2	0.7	4.3
23	HII	4.7	2.1	21.1	0.2	0.9	0.1	0.5	1.7
24	HII	4.9	2.1	32.1	0.4	1.0	0.2	0.5	1.9
25	diffuse HII	4.4	4.5	27.6	0.5	1.2	0.2	0.3	4.3
26	diffuse HII	4.3	3.3	20.4	0.3	0.5	0.1	0.2	2.9
27	HII	4.8	5.4	8.4	0.6	12.0	0.8	2.8	4.3
28	YSO	4.9	10.8	27.6	1.3	4.7	0.1	0.3	14.3
29	HII	4.4	5.6	47.3	0.9	5.8	0.1	0.9	6.8
30	HII	4.4	2.7	19.3	0.3	2.3	0.3	1.1	2.0
31	YSO	5.0	2.0	21.6	0.1	0.3	0.1	0.2	1.6
32	HII	5.0	2.9	31.1	0.5	2.9	0.2	1.1	2.7
33	HII	5.0	2.1	31.2	0.2	2.0	0.2	1.2	1.7
34	diffuse HII	4.7	3.5	42.2	0.2	2.9	0.1	0.9	3.2
35	HII	5.0	1.7	36.0	0.2	2.4	0.3	1.8	1.4
36	diffuse HII	4.6	3.0	12.7	0.3	2.8	0.1	1.1	2.6
37	diffuse HII	4.6	5.3	31.3	0.1	1.9	0.0	0.4	4.5
38	HII	5.0	3.5	25.3	0.2	0.7	0.1	0.2	2.9
39	diffuse HII	4.6	5.6	40.8	0.3	1.6	0.1	0.3	5.2
40	diffuse HII	4.6	4.8	24.3	0.4	2.5	0.1	0.6	4.4
41	YSO	5.0	4.8	16.7	0.5	1.8	0.1	0.4	4.5
42	HII	4.4	5.0	34.4	0.6	3.8	0.1	0.8	5.1
43	YSO	5.0	2.4	14.8	0.6	1.6	0.3	0.7	2.2
44	YSO	5.0	3.0	21.6	0.4	1.2	0.2	0.5	2.6
45	YSO	5.0	2.9	35.7	0.6	2.2	0.3	0.7	2.9
46	HII	4.4	4.8	20.3	0.4	1.6	0.1	0.4	4.3
47	HII	4.5	5.6	27.3	0.4	1.5	0.1	0.3	5.3
48	diffuse HII	4.4	2.5	13.6	0.2	0.8	0.2	0.4	1.9
49	HII	4.4	3.4	33.6	0.5	2.6	0.2	0.8	3.3
50	HII	5.0	4.2	44.0	1.1	8.8	0.2	1.6	5.4
51	HII	5.0	1.3	34.7	0.4	2.6	0.3	2.3	1.1
52	diffuse HII	4.7	3.3	32.2	0.3	0.9	0.1	0.3	2.9
53	HII	4.6	5.2	31.2	0.5	1.7	0.1	0.3	5.1
54	HII	5.1	6.5	24.4	0.2	1.3	0.1	0.2	5.5
55	YSO	5.1	3.6	30.9	0.4	2.3	0.2	0.7	3.3
56	HII	5.1	4.9	35.3	0.5	2.7	0.1	0.6	4.8

Notes. The superscripts 13 and 18 mean ^{13}CO and C^{18}O, respectively.

Table A.2. continued.

#	Type	D_{gal} (kpc)	$I^{13/18}$	T_{ex} (K)	τ^{13}	N^{13} ($\times 10^{16}$ cm^{-2})	τ^{18}	N^{18} ($\times 10^{16}$ cm^{-2})	$X^{13/18}$
57	HII	5.0	4.9	22.8	0.4	2.0	0.1	0.5	4.4
58	HII	4.6	2.7	31.3	1.3	12.6	0.4	3.8	3.3
59	HII	5.2	2.8	29.6	0.3	2.3	0.2	1.0	2.4
60	HII	4.7	1.8	13.3	0.5	1.7	0.5	1.2	1.4
61	diffuse HII	4.7	4.0	17.2	0.3	0.8	0.2	0.3	3.1
62	YSO	5.1	3.8	24.6	0.5	1.5	0.2	0.4	3.5
63	YSO	4.7	4.9	27.7	0.3	1.4	0.1	0.3	4.2
64	HII	5.3	2.4	30.0	0.2	0.9	0.1	0.4	2.1
65	diffuse HII	5.6	2.7	21.5	0.7	2.1	0.2	0.8	2.6
66	HII	4.7	2.6	44.1	0.9	6.9	0.6	2.6	2.6
67	diffuse HII	5.8	1.6	16.6	0.1	0.8	0.1	0.6	1.2
68	diffuse HII	5.8	2.9	34.3	1.9	8.6	0.4	2.0	4.4
69	HII	6.2	1.6	8.8	3.3	8.8	0.5	2.3	3.8
70	HII	5.1	10.5	24.4	0.5	1.4	0.1	0.1	9.8
71	YSO	5.4	2.3	15.3	0.7	1.8	0.4	0.9	2.0
72	HII	6.0	4.8	11.5	2.4	8.1	0.5	1.0	7.9
73	HII	5.4	3.0	36.2	0.9	3.5	0.3	1.0	3.3
74	HII	6.0	3.8	31.4	0.6	3.0	0.2	0.8	3.7
75	HII	6.0	4.3	43.3	0.7	6.7	0.2	1.4	4.7
76	HII	6.0	3.8	23.6	0.7	3.6	0.2	1.0	3.8
77	YSO	6.0	3.4	39.1	0.6	1.7	0.2	0.5	3.4
78	HII	6.0	5.4	31.0	1.1	3.3	0.2	0.5	6.5
79	HII	6.1	4.6	47.4	0.7	3.8	0.1	0.7	5.0
80	YSO	5.2	1.6	27.2	0.3	1.1	0.2	0.9	1.3
81	HII	6.3	4.3	19.3	0.6	1.8	0.2	0.5	3.9
82	diffuse HII	5.7	2.5	29.8	0.4	2.6	0.2	1.2	2.2
83	HII	6.0	2.9	25.3	0.4	2.2	0.2	0.9	2.5
84	HII	5.9	3.8	34.1	0.8	7.8	0.2	1.9	4.2
85	HII	5.8	4.0	29.5	0.5	2.0	0.3	0.6	3.6
86	HII	6.2	5.1	24.4	0.8	3.0	0.2	0.6	5.4
87	YSO	6.6	4.3	29.7	0.5	1.9	0.2	0.5	4.0
88	HII	5.9	1.6	18.9	0.4	1.5	0.3	1.1	1.3
89	YSO	5.9	1.1	25.6	0.3	1.1	0.3	1.3	0.8
90	YSO	6.3	3.0	13.8	0.2	0.9	0.1	0.4	2.4
91	HII	6.0	4.9	20.4	0.4	2.0	0.1	0.5	4.3
92	HII	5.5	2.4	10.4	0.4	1.1	0.2	0.5	2.2
93	YSO	5.5	3.6	27.2	0.5	2.5	0.2	0.8	3.3
94	HII	6.9	1.5	17.2	0.2	0.9	0.2	0.8	1.2
95	HII	6.1	2.0	15.9	0.1	0.5	0.1	0.3	1.5
96	HII	6.1	5.4	15.7	1.4	3.4	0.2	0.5	6.9
97	HII	7.6	5.7	15.9	0.8	2.7	0.1	0.4	6.0
98	HII	5.8	5.8	12.6	0.5	1.2	0.1	0.2	5.4
99	HII	7.6	5.5	49.0	0.7	7.1	0.1	1.1	6.4
100	HII	7.6	6.5	43.7	0.9	6.8	0.1	0.9	7.7
101	diffuse HII	8.3	3.8	31.8	0.3	2.1	0.1	0.6	3.4
102	HII	7.6	3.4	45.8	0.5	7.2	0.4	2.3	3.1
103	HII	7.6	1.4	44.8	0.7	11.6	0.4	8.5	1.4
104	diffuse HII	8.3	12.3	46.1	0.5	6.2	0.1	0.5	12.7
105	HII	6.2	2.9	25.6	0.3	1.4	0.2	0.5	2.5
106	HII	6.6	2.5	25.6	0.9	6.9	0.4	2.8	2.4
107	YSO	6.5	2.5	10.7	0.4	1.3	0.2	0.6	2.2
108	YSO	5.9	3.1	36.0	0.3	1.0	0.1	0.4	2.8
109	HII	6.2	3.7	21.5	0.3	2.4	0.2	0.7	3.2
110	HII	6.2	0.6	42.0	0.4	1.7	0.3	3.1	0.6
111	HII	6.2	3.1	32.2	0.3	1.2	0.1	0.4	2.8
112	HII	6.2	4.6	48.0	1.1	8.6	0.2	1.4	6.0
113	HII	6.1	3.4	25.0	0.6	3.3	0.2	1.0	3.2
114	diffuse HII	6.1	6.8	38.3	0.5	2.4	0.1	0.3	7.1